Modular nanostructure design of DX-tile DNA nano-stars (DX-DNAns) controls self-organization and force propagation of DX-based DNA Hydrogels yielding a soft matter metamaterial with programmable viscoelastic properties and integrated functionalization

Joshua Bush[1,2,3*]

1 Department of Bioengineering, George Mason University, Fairfax, VA 22030

2 Department of Mechanical Engineering, Old Dominion University, Norfolk, VA 23529

3 Department of Biomedical Engineering, Stony Brook University, Stony Brook, NY 11794

* Corresponding Author

Abstract

Deoxyribonucleic Acids (DNA) have been used since 1982 to form nanostructures with precisely tunable features, shapes, responses, etc. Some of the most basic structures, DNA nanostars (DNAns) have been used to form soft matter hydrogels with unique functionalizations and responses to soluble stimuli as well as physical cues. Notably these studies use 'arms' comprising a single duplex whereas more complex nanostructures, DNA origami, can have a multitude of duplexes bundled together to produce different structural properties. Herein I introduce DNAns bundling two duplexes together, commonly known as the double crossover (DX) motif to enable multi scale mechanical design of hydrogels with interchangeable strands, i.e. modular DX-DNAns hydrogels. This is achieved by rational design of the internal structure to coordinate the propagation of forces both within and across the different motifs driving unique organizational aspects which produce specific viscoelastic features, as evidenced by bulk-scale rheological profiles herein. This work begins to bridge the broad range of complexities available with DNA origami based nanostructures to the more application based potentials for macro-scale nanostructured materials with specified functionalizations. Particularly I elucidate the versatility of this method by implementing a DNA based pH response motif, i-motif, which has thus far only enabled switchable mechanical properties from the gel-to-sol states but herein there are graded changes in mechanistic properties while sustaining the gel

state, a feat which has only been achieved via strand displacement in DNAns hydrogels thus far. Demonstrating the breadth of new possibilities for DNA hydrogels with the extensive functionality of bundled duplexes used in DNA Origami thus seeding the bridge to a fundamental gap in the field by pinpointing this new fundamental design factor.

1. Main

Deoxyribonucleic acid (DNA) based hydrogels have been formulated via rolling chain amplification (RCA), hybridization of short oligonucleotides (~20 nucleotides [nt]), and covalent functionalization of polymers using DNA as a crosslinker. Each approach yields unique mechanical properties as detailed in recent reviews[1–5]. In this work I build upon the common DNA nanostar (DNAns) design which applies DNA nanotechnology to form a multi-armed star with a vertex and 3-6 arms. Most often 3 arms are used and consists of a single DNA duplex per arm, which is commonly on the order of 20 nts (~7nm) in length.[1,6–9] These DNAns hydrogels are shown to be remarkably soft often less than a few hundred Pascals (Pa) owing to the flexibility of DNA and weak hydrogen-bonding crosslinks.[1,9] With this work I aim to expand the versatility of DNAns hydrogels by integrating the double crossover (DX)-tile design motif to yield DX-DNAns. The DX-tile design motif is used to generate wireframe DNA nanostructures and affords multiple sites for functionalization via folding with modified oligonucleotides.[10,11]Using the DX-tile motif to generate DNA hydrogels enables additional degrees of freedom with regards to nanostructural design and functionalization as demonstrated herein.

In this work I alter the DX-DNAns design to tune the viscoelasticity and formation of the gel while also introducing pH-switchable analogues. Additionally, I demonstrate the potential for functionalization of DX-DNAns gels by incorporating an i-motif based pH sensor. Notably, tunable viscoelasticity and functionalization potential yield a suitable biomaterial for studying viscoelastic influences on mechanobiology[12–14] and/or incorporation of DNA-based tension sensors (Supplementary Table 5).[15,15,16] DNA origami has enabled the nanoscale organization of signaling ligands[17–19] for which these nanostructures may be readily anchored to DX-DNAns gels by the addition of an overhang binding staple.

Furthermore, my approach enables the development of macroscale materials with nano-templated dyes[20–22] and/or optical nanoparticles[23–26] which expands the DNA nanotechnology tool kit for developing novel plasmonic[25,27–30], light-harvesting[31–34], and opto-electronic[35–37] materials. DNA origami structures are currently limited to ~200nm as defined by the scaffold length. The production of DNA origami scaffolds is currently costly[38] and proves a fundamental limitation to the production of large-scale materials using DNA origami, thus nanostructured DNA hydrogels are synthesized from synthetic oligonucleotides. Although, DNA origami structures have been crosslinked to yield larger micron-scale structures in solution.[39–41] However it is not clear to what extent these nanostructures can be linked to form macroscale materials and whether structures or crosslinks will remain stable as the magnitude of lattice vibrations scale. DX-DNAns hydrogels enable a modality to begin exploring this frontier further, with a principle design feature demonstrated herein.

Specifically, in this work I explore the influence of DNA motif concentration and hybridizing DNA linkers, as well as base-stacking crosslinks, on bulk viscoelasticity and hydrogel formation before and after thermal annealing of the hydrogel. I demonstrate that the nanostructure may be designed to alter the formation dynamics, and the respective influence of each linker is highly dependent upon the nick and crossover location of the internal staple strand. In order to dynamically switch between these design features I incorporate a multi-strand i-motif as a pseudo-crossover within the DX-DNAns arm or the linker. Prior applications of i-motifs within DNAns hydrogels only enable gel-sol transition as the unformed i-motif sequence yields a high degree of flexibility across the linker when integrated along a single strand. Finally, I demonstrate the potential for chemical functionalization of the nanostructures by integrating a fluorescent DNA-based pH sensor by interchanging the staple strands with modified oligonucleotides.

1.1 Nanostructured DX-DNAns Hydrogels

The design for these gels was strongly inspired by one particular study in which it was found that for a DNA hydrogel synonymous with a linear polymer containing multiple crosslinking sites, the inverse of ‘direct expectation’ was true. Namely, incorporating flexibility into DNA design itself enabled an

increased storage modulus.[42] The fragility of DNA hydrogel crosslinking being solely dependent upon multiple structured hydrogen bonds presents a unique situation for hydrogels. Specifically the structure and nature of the DNA-DNA interactions enables a uniquely enhanced mode of hydrogen bond based crosslinking while synonymously being stabilized by fluctuant pi-pi orbital stacking interactions[43,44] effecting a loose mode of rigidity within the DNA duplex itself [36], an 'accordion-like' mode if you will. This enables coherent high-frequency modes[45–47] with a 'perpetual dynamism' that may be likened to a linear system of springs and masses, namely when coupled with resonant nanostructure design as done here. By incorporating flexibility within the design this mode of 'vibrational rigidity' is free to fluctuate while enacting a sort of 'driven stiffening' as it returns to its taut state and perhaps simultaneously accruing the strain energy within the 'resonant masses' themselves which would be most analogous to the electron-phonon effect[45–50]. When coupled between multiple subunits (arms and linkers), a mode of programmable nanoscale force propagation is available with definable nodes, for which the 3-way junction was chosen here for simplicity of highlighting the arm and linker influences.

Notably rotational symmetry is applied for strand sequence design to enhance folding efficiency at the higher DNA concentrations required for gel formation relative to those used standardly for DNA nanostructures and in contrast to the excess staples required for folding of DNA Origami. In this study pliant and stiff arms are studied along with four linker variations and two i-motif based switchable analogues to demonstrate the requirement of the pliant arm design for adequate self-organization to form a viable and stable gel-like structure with consistent programmable properties. The design of i-motif analogues were inspired and tempered by previous works which looked at the anchoring influences on i-motif formation.[51,52] Notably folding and unfolding of i-motifs occurs at an intrinsic time-scale of ~100ms in response to a change in pH[53] independent of forces enacted by vibrations of the gel structure itself which also showed unique response features on the same timescale independent of the i-motifs presence.

The DX-DNAns designs presented herein have been designed to be entirely modular such that one strand may be exchanged to produce completely different properties in some cases and sets of strands may

be exchanged to produce alternate properties. Notably the 3-arm DX-DNAns may also be expanded to multiple valencies such as 4, 5, and 6 by exchanging a few of the 4 core strands with alternate sets and utilizing the same toolkit of strands for the arm and linker variations (Supplementary Figure 3). Effectively with only a select subset of DNA strands, a multitude of design motif variations may be formed. While this study focuses on the internal design and linker variations for finely tunable elasticity it is expected that the storage moduli can increase by an order of magnitude to ~1kPa for 6-arm junctions as described in an exceptionally well-focused study in 2019[54] for which some key points to this work were described in my review[1]. Interestingly their study showed a stark increase in storage moduli from the 4 to 5 arm motifs suggesting that combinations of multi-arm motifs will enable a finely tunable storage modulus range across an order of magnitude range in supplement to finely tunable viscoelastic properties, along with the coupled and tunable nanostructural force propagation. Finally, the same design concept can be applied to an 'extended arm' design (Supplementary Figure 3) which opens an entirely new modular toolkit for nanostructural design while utilizing the same core strands for valencies of 3, 4, 5, 6 (Supplementary Table 4), for which new degrees of complexity and variation may be introduced.

1.2 Linker Design Alters Bulk Viscoelastic Properties

I investigated four different linker designs, Long (Lo), Long mismatch (Lm), Short (Sh), and Stacked (St) as depicted in Figure 2a. I investigated the frequency-dependent rheological properties of each linker at 3 different DX-DNAns motif concentrations of 30, 60, 90 uM, selected to be nearest to the commonly used 1.0, 1.5, 2.0% w/v. To observe the formation dependent conditions, I melted and annealed the gel from 25-to-55-to-25ºC with a 5-minute transition between temperatures. At 30 uM pre-annealing, I observed a sol-state for all linkers with the pliant arm (Fig. 2b i, v, viii), except the short linkers which displayed a storage modulus <10 Pa (Fig. 2b iii) though consistently formed a gel state, as determined by G'>G". Post-annealing the Lo linker formed a gel state with moduli ~20 Pa (Fig. 2b ii), whereas the Lm linker remained in the sol state (Fig. 2b vi). This is due to the flexibility in the linker diminishing the long-range rigidity of the loosely percolated network formed at this low concentration. The short linker design

yielded a decrease in storage moduli post-annealing (Fig. 2b vi), which I also observed at the higher concentrations (Fig. 2b xiv, xvii). This suggests that the decrease in storage moduli post-annealing may be attributed to the faster binding kinetics of the Sh linker which can drive the network towards the formation of aggregates during the specific annealing conditions used, while more rapid cooling may produce different results. The stacked linker at 30 uM post-annealing reached a gel-state with a 2 Pa storage modulus (Fig. 2b viii). This demonstrates the contribution of structural rigidity at the linker interface to stiffen the percolating network. Interestingly the structure appears to facture or disintegrate at frequencies greater than $3x10^3$ rads/s (Fig. 2b viii). A similar phenomenon is observed for the stiffer Lo linkers (Fig. 2b I, ii).

At the mid-range concentration of 60 uM I observed all linkers to form a gel, both pre- and post-annealing (Fig. 2b ix-xvi). Pre-annealing the Lo-ON-60uM and Lm-ON-60uM gels demonstrated a similar storage modulus ~100 Pa whereas the Lm-ON-60uM demonstrated a similar loss modulus at frequencies greater than 10 rad/s but greater dissipation at lower frequencies evidenced by the increased loss modulus (Fig. 2b ix, xi). The greater low frequency loss modulus in the Lm-ON-60uM gel indicates a faster relaxation time. Which may be attributed to the lower affinity of the Lm linker with only 14 hybridizing base pairs (bp) in comparison to 21 bp within the Lo linker. Alternatively, the flexibility in the Lm linker may afford an additional means of configurative stress dissipation which is only apparent at lower frequencies due to the time dependence for structural reconfiguration. The short linker demonstrated a similar, but slightly lesser, storage modulus as expected due to the lower affinity of the Sh linker with only 7bp (Fig. 2b xiii, xiv). The lower affinity of the Sh linker also yields faster kinetics resulting in glassy behavior, as evidenced by the linear profile of the loss modulus below 100 rad/s (Fig. 2b xiii). The St linker forms a softer gel with a storage modulus ~10 Pa attributed to the weaker linker affinity (Fig. 2b xv, xvi). However, post-annealing the storage modulus remains the same but the loss modulus decreases indicating a decreased rate of ruptured cross links. The greater stability of the crosslinks indicates that annealing reorders the network to better distribute stress. The influence of the improved efficiency of stress

distribution upon the loss modulus is accentuated by the rigidity, and resultant fragility, of the St linker which lacks the potential for stress dissipation via deformation.

At the 90 uM concentration I observe a slight increase in moduli for all 4 linkers (Fig. 2b xvii-xxiv). The Lm-ON-90uM, Sh-ON-90uM, and St-ON-90uM hydrogels demonstrate the same behaviors observed at 60 uM (Fig. 2b xix-xxiv). Whereas the Lo-ON-90uM hydrogel demonstrates a notable increase in sample deviation (Fig. 2b xvii-xviii) which may be explained by the rigidity of the long linker and concurrent slower kinetics. The rigidity of the linker limits the ability of localized domains to be compressed and reoriented at higher concentrations driving the system to form interpenetrating percolated networks, yielding greater fluctuations in the network's structure between samples. Alternatively, the slower linker kinetics of the Lo linker may trap saturated domains yielding a greater sample to sample variation in comparison with the Lo-ON-60uM.

The rigidity of the long linker can be further validated in Figure 2c by observing the sudden increase in the loss modulus at a strain of <1%. Whereas the Lm linker demonstrates a smoother increase in the loss modulus from ~2-20% strain (Fig. 2c ii), indicating a greater distribution of network structures afforded by the flexibility in the linker. Given their faster kinetics and 'glassy'-response, short and stacked linker can both undergo considerably greater deformation before a change in the loss modulus is observed at ~10 and 30% strain, respectively (Fig. 2c iii, iv). This linker dependent deformability and kinetic dependence is further validated by the increasing yield strains of 30, 50, 100, and 200% for the Lo, Lm, Sh, and St linkers, respectively (Fig 2c i-iv).

1.3 Stiff Nanostructure Alter Bulk Formation

Pure DNA hydrogels exhibit the fundamental limitation of innate crosslinks containing only hydrogen bonds when hybridization is used, in contrast with covalent functionalization which may negate the biocompatibility. While DNA nanotechnology may allow the design of variate rigid structures, the bulk material properties are limited by the cross linkers ability to sustain stress without rupture. The first

approach would be to increase the affinity of the linkers to yield a stiffer gel, however this change may significantly alter the dynamics of the gel. Therefore, I designed the pliant arm, without a central crossover, to buckle and afford a reversible means of stress propagation through the network, alleviating the stress at the crosslinkers. To validate this approach, I also designed a stiff arm with an internal crossover (Fig. 3a) for comparison and characterized both when using each of the 4 linkers to form a hydrogel with DX-DNAns motif concentration of 60 uM.

In figure 3a I observe the frequency-dependent rheology of the stiff-arm design pre- and post-annealing. Pre-annealing, only Lo-X-60uM forms a gel-state (Fig. 3A i) given the linkers ability to sustain stress and decreased flexibility which limits the compaction of crosslinked motifs yielding a more expansive network relative to the Lm-X-60uM, Sh-X-60uM, and St-X-60uM before annealing (Fig. 3a iii, , v, vii). After annealing to approach the networks equilibrium state, each motif forms a gel with moduli magnitude and frequency dependencies similar to their pliant arm counter parts in figure 2b (ii, vi, viii, x, xii, xiv, xvi). Lo-X-60uM, Sh-X-60uM, and St-X-60uM show a considerable increase in sample deviation as compared to their pliant arm counterparts post-annealing. However, the Lm-X-60uM retains a lesser degree of sample variation (Fig. 2b iv) which may be the result of the flexibility within the Lm linker enabling a more uniformly percolated network.

I analyze the gels' melting/annealing profiles in Figure 3b for all 4 linkers at 60 uM with stiff versus pliant arms (Fig. 3B). The pliant arm DX-DNAns gels demonstrate similar moduli pre- and post-annealing (Figure 3B i-iv) indicating an equilibrium state is reached without thermal annealing. The stiff arm shows an increase in moduli for each linker post-annealing (Figure 3B v-viii), indicating thermal annealing yields a more ordered network. Interestingly, Lm-X-60uM is the only design that remains in the gel state through the melting/annealing process (Fig. 3 B vi) as a result of the conformational flexibility in the linker though the increased linker melting temperature is dependent upon the internal nanostructural design (i.e. rigid vs. pliant arm). All designs exhibit a decrease in the storage modulus upon initial heating (Fig. 3B i-viii), whereas the initial response of the loss modulus is dependent on the apparent arm rigidity. For the stiff-arm

gels, the loss modulus immediately decreases (Fig. 3B v-viii) while the pliant arm exhibits an increase in the loss modulus for each hybridizing linker (Lo, Lm, Sh – Fig. 3B I, ii, iii), but not the St linker (Fig, 3B iv). This initial increase in the loss modulus may be the result of the pliant arm's ability to dissipate stress alone, however this increase is not observed in the stacked linker. The notable difference of the stacked linker is that it may only adopt a linear configuration and therefore the steric distribution of crosslinks is narrow. Whereas the flexibility and dual strand nature of the other linkers afford a broader range of steric conformations for the crosslinks. The pliant arm's ability to deform in response to stress from a connected DX-DNAns is thus dependent on the alignment of the connected arms. As a result, stress is concentrated at sterically unfavorable crosslinks while it is propagated across aligned crosslinks, generating a sterically-dependent bimodal distribution of effective crosslinker strength. In figure 3b, the initial increase in the loss modulus demonstrates the increased rate of rupture for the misaligned crosslinks upon heat injection. By concentrating stress at sterically unfavorable crosslinks the network is then able to self-organize via survival of the fittest crosslinks, similar to the effect of annealing. This degree of self-organization is apparent by observing the ability for each crosslinker to gel pre-annealing, with considerably lower sample deviation, when the pliant arm is used. The nonlinear change in loss modulus with respect to temperature may also be the result of 'chaotic resonances' or 'pre-stress' within the system itself, perhaps localized to certain sub-networks formed, which would then reach spontaneous points of rupture within the system as an immediate response to the heat injection as opposed to a change in temperature itself.

1.4 pH-switchable Analogues

To further validate DX-DNAns driven assembly via nanostructured force propagation, I designed pH switchable analogues which enable the reversible insertion of dissipative elements within the arm and the crosslinker (Fig. 4a). The dissipative element being an i-motif in this particular example, which crosslinks both duplexes within the arm, forming a pseudo-crossover, or within the crosslinker, converting a mismatch linker into a long linker with a pseudo-crossover between the linker duplexes. In Figure 4Biii, I observe that the Lo-iC motif at pH 8.0 (Lo-iCpH8) and concentration of 60uM (Lo-iCpH8-60uM)

replicates the rheology profile of its analogue, the Lo-PL-60uM in figure 2Bixx. Both pre and post-annealing rheology profiles are similar, as expected for the pliant arm and long linker at this concentration. A key difference to note is the post-annealing loss modulus is different for the i-motif containing structure at pH 8.0. The presence of the poly-C overhangs may act as a dissipative defect for force propagation along the arms, resulting in a smoother loss modulus relative to Lo-PL-60uM (Fig. 2b x). Alternatively, the i-motif may still be transiently forming for short timescales at high pH, thus acting as another dissipative mechanism and disrupting the unique frequency dependency of the loss modulus for Lo-PL-60uM (Fig, 2b x). Alternatively, the Lo-iC motif at pH 5.0 (Lo-iCpH5) contains the formed i-motif within the arm, crossing each duplex, of the DX-DNAns. The analogue for this state is Lo-X (Fig 3a iii-iv) which contains the same Long linker and contains a crossover at the same location as the i-motif within the DX-tile arm. For Lo-iCpH5-60uM (Fig 4a iii, iv) I observe a similar profile to its analogues both pre- and post- annealing (Fig 3a iii-iv), however the pre-annealing moduli are nearly an order of magnitude lower than the post-annealing moduli. This difference in the pre-to-post annealing moduli demonstrates again the need for pliancy in the arm to drive self-organization at lower temperatures, demonstrated by a dissipative crossover versus a fixed crossover.

Next, I observe the LC-ON motif at pH 8.0 (LC-ONpH8) (Fig 4a v, vi), whose analogue is the Lm-ON (Figure 2b ix, x) and for which I expect similar pre- and post-annealing rheology profiles given its pliant arm and potential for self-organization. However, while LC-ONpH8 and Lm-ON-60uM have similar pre/post annealing rheology profiles, the LC-ONpH8 gel's moduli are approximately 4-fold less. Notably for the LC-ON motif there are no additional base overhangs, as required for the arm in the Lo-iC motif, making it structurally identical to its analogue Lm-ON. The difference being the exchange of 3 poly-T mismatches being converted to 3 cytosine residues on each of the four strands contained within the DX-based linker (Fig 4b). Suggesting the difference in moduli to be the result of the cytosine interactions forming short lifetime i-motifs at high pH[55]. Although, this would intuitively suggest an increase in the moduli given its potential to rigidify the linker and reversibly dissipate stress. Alternatively, the transient

formation of this i-motif may disrupt the soft (low-frequency) vibrational modes within the network which have been shown to be proportional with shear moduli[56] and would justify a decrease in the moduli as the linker's ability to propagate stress is diminished. Whereas for the LC-ON motif at pH 5.0 (LC-ONpH5) (Fig 4a vii-viii) I observe a similarity with an unanticipated analogue. The structural analogue for LC-ONpH5 is Lo-ON, however a structural dissimilarity is that LC-ON-pH5 contains a pseudo-crossover within the linker (Fig 4a – last schematic). Intriguingly I observe similar rheology profiles with the Lm-X-60uM, which contains a crossover in the arm and flexibility in the linker, thus producing defects at different locations on the structure yields similar formation profiles and moduli. In sum, the location of the 'defect', or crossover, is not as critical as the existence itself. A notable difference for LC3-ONpH5 is the inversion of the storage moduli trend which continues increasing after 10 rad/s (Fig 4a viii), notably a similar timescale to the folding/unfolding rate in response to pH change[57]. The increase in storage moduli after minimum loss moduli may result from the i-motif crosslinker's ability to dissipate energy reversibly without complete rupture of the crosslink. This reversible energy dissipation would warrant the observed increase in both storage and loss moduli beyond the timescale of force propagation through the DX-DNAns arm, ~ 10 rad/s (Fig 4a viii). Now comparing the i-motif as a crossover defect I have observed similar rheology profiles to each analogue, however when the i-motif is formed at pH 5.0 I observe significantly less sample variation in moduli (Fig 4 a iv,viii) relative to the stiff-arm analogues. Considering the potential for the i-motif to act as a reversibly dissipative crossover, the decreased sample variation suggests an increased potential for network homogeneity via improved distribution and dissipation of prestress.

1.5 Integrated DNA-based pH Sensor

To demonstrate the potential for functionalization of these DX-DNAns hydrogel I designed an integrated pH sensor which forms an i-motif at low-pH by bringing a fluorescent dye, Atto647N, and quencher, Iowa Black ® RQ, into close proximity (Supplementary Figure 2). The Atto647N dye was chosen for its broad fluorescence stability from pH 2-10.[58] At high pH the sensor fluorescence is maximal and decreases with lower pH as the i-motif forms bringing the fluorescent dye closer to the quencher molecule

and thus diminishing fluorescent output via Förster Resonance Energy Transfer (FRET). For the integrated sensor used here I observe a transition at ~pH 6.4 across ~0.6 pH units (Supplementary Figure 2). Similarly, this same integration of functional strands within the structure may be applied for K^+ sensors or Mechanosensors (Supplementary Table 5).

2. Outlook

DNA nanotechnology has enabled access to unprecedented control over molecular and nanoarchitecture design. However, the development of macroscale materials using purely DNA has been limited to duplex DNAns and long hybridizing DNA with little-to-no exploration into more complex structures and design features for macroscale 3D functional nano materials. Here I demonstrate that nanostructure design afforded by DNA nanotechnology has the potential to produce programmable self-organizing macroscale nanomaterials. DX-DNAns hydrogels offer a unique medium to study soft matter physics with unprecedented design control[59–64]. The biocompatibility of these gels makes them useful as biomaterials and opens potential for replicating and engineering the mechanics and dynamics of biomaterials for further study and application of mechanotransducive pathways relative to native biomaterial mechanics. The self-driven organization of this material from nano-to-macro scale yields it a desirable candidate for the production of nano-organized plasmonic materials[65–70].

3. Methods and Materials

3.1 DX-DNAns Design

DX-DNAns were first designed by hand on 9/30/2019 during my Polymer Chemistry class then rendered in Tiamat to produce specific sequence files. Alterations were generally made from the original file to produce variations with identical sequence pairing but altered nick placement, linker lengths/binding, and inclusion of functional motifs for interchangeable or 'modular' design potentials.

3.2 Folding of DX-DNAns

DX-DNAns were folded in !X TAE buffer with 12mM Mg^{++} by annealing over night from 95ºC->25ºC. DX-DNAns with the functional i-motif were folded in 1X PBS titrated to the appropriate pH with HCl and NaOH solutions. All DNA strands used were originally sourced from Integrated DNA Technologies (IDT).

3.3 Rheological Studies

Rheology measurements were conducted using an MCR302 rheometer with 25mm parallel plates. Frequency sweeps were conducted at a strain of 1%. Strain sweeps were conducted at a frequency of 10 rad/s. Thermal profiles were assessed at a strain of 1% with a frequency of 10 rad/s while heating and cooling from 25ºC->55ºC->25ºC with a 2-mintue hold at 55ºC and a 5-minute hold at 25ºC both pre- and post- thermal ramping.

Acknowledgements

I would like to acknowledge Remi Veneziano for his mentorship and providing basic supplies as well as Venkat Maruthamuthu for providing access to a rheometer. I would like to acknowledge both Remi and Jeffrey Moran for their general input on the early stage of the manuscript.

Conflict of Interests

I have no conflict of interest to declare.

References

1. Bush, J., Hu, C.-H. & Veneziano, R. Mechanical Properties of DNA Hydrogels: Towards Highly Programmable Biomaterials. *Appl. Sci.* **11**, 1885 (2021).
2. Cao, D., Xie, Y. & Song, J. DNA Hydrogels in the Perspective of Mechanical Properties. *Macromol. Rapid Commun.* **n/a**, 2200281.

3. Wu, R. *et al.* DNA hydrogels and their derivatives in biomedical engineering applications. *J. Nanobiotechnology* **22**, 518 (2024).
4. Yang, Z.-H. *et al.* Research advancement of DNA-based intelligent hydrogels: Manufacture, characteristics, application of disease diagnosis and treatment. *Chin. Chem. Lett.* **35**, 109558 (2024).
5. Zhu, Z. *et al.* DNA Hydrogels in Tissue Engineering: From Molecular Design to Next-Generation Biomedical Applications. *Adv. Healthc. Mater.* **14**, 2500192 (2025).
6. Morya, V., Walia, S., Mandal, B. B., Ghoroi, C. & Bhatia, D. Functional DNA Based Hydrogels: Development, Properties and Biological Applications. *ACS Biomater. Sci. Eng.* **6**, 6021–6035 (2020).
7. Biomedical Applications of DNA-Based Hydrogels - Gačanin - 2020 - Advanced Functional Materials - Wiley Online Library. https://advanced.onlinelibrary.wiley.com/doi/full/10.1002/adfm.201906253.
8. Li, F., Lyu, D., Liu, S. & Guo, W. DNA Hydrogels and Microgels for Biosensing and Biomedical Applications. *Adv. Mater. Deerfield Beach Fla* **32**, e1806538 (2020).
9. Wang, Y. *et al.* Mechanical properties modulation and biological applications of DNA hydrogels. *Adv. Sens. Energy Mater.* **3**, 100113 (2024).
10. Zhang, Y., Yang, D., Wang, P. & Ke, Y. Building Large DNA Bundles via Controlled Hierarchical Assembly of DNA Tubes. *ACS Nano* **17**, 10486–10495 (2023).
11. Hill, A. C. & Hall, J. High-order structures from nucleic acids for biomedical applications. *Mater. Chem. Front.* **4**, 1074–1088 (2020).
12. Lin, Z. *et al.* Mechanobiological modeling of viscoelasticity in soft tissue growth and morphogenesis. *J. Mech. Phys. Solids* **196**, 106032 (2025).
13. Chaudhuri, O., Cooper-White, J., Janmey, P. A., Mooney, D. J. & Shenoy, V. B. Effects of extracellular matrix viscoelasticity on cellular behaviour. *Nature* **584**, 535–546 (2020).
14. Egr1 is a 3D matrix–specific mediator of mechanosensitive stem cell lineage commitment | Science Advances. https://www.science.org/doi/10.1126/sciadv.abm4646.

15. Schlichthaerle, T., Lindner, C. & Jungmann, R. Super-resolved visualization of single DNA-based tension sensors in cell adhesion. *Nat. Commun.* **12**, 2510 (2021).

16. Zhang, Y., Ge, C., Zhu, C. & Salaita, K. DNA-based digital tension probes reveal integrin forces during early cell adhesion. *Nat. Commun.* **5**, 5167 (2014).

17. Teodori, L. *et al.* Nanoscale Precise Stamping of Biomolecule Patterns Using DNA Origami. *ACS Nano* https://doi.org/10.1021/acsnano.5c07651 (2025) doi:10.1021/acsnano.5c07651.

18. Wu, Y. *et al.* Precise construction of DNA origami-based materials for functional regulation on biological interface. *Smart Mol.* **2**, e20230032 (2024).

19. Hou, Y. & Treanor, B. DNA origami: Interrogating the nano-landscape of immune receptor activation. *Biophys. J.* **123**, 2211–2223 (2024).

20. Cervantes-Salguero, K. *et al.* Minimizing Structural Heterogeneity in DNA Self-Assembled Dye Templating via DNA Origami-Tuned Conformations. *Langmuir* **40**, 10195–10207 (2024).

21. Gorman, J. *et al.* Sculpting photoproducts with DNA origami. *Chem* **10**, 1553–1575 (2024).

22. Zhan, P. *et al.* Recent Advances in DNA Origami-Engineered Nanomaterials and Applications. *Chem. Rev.* **123**, 3976–4050 (2023).

23. Shen, B., Kostiainen, M. A. & Linko, V. DNA Origami Nanophotonics and Plasmonics at Interfaces. *Langmuir* **34**, 14911–14920 (2018).

24. Dass, M., Gür, F. N., Kołątaj, K., Urban, M. J. & Liedl, T. DNA Origami-Enabled Plasmonic Sensing. *J. Phys. Chem. C* **125**, 5969–5981 (2021).

25. Shen, B. *et al.* Plasmonic nanostructures through DNA-assisted lithography. *Sci. Adv.* **4**, eaap8978 (2018).

26. Kuzyk, A. *et al.* DNA-based self-assembly of chiral plasmonic nanostructures with tailored optical response. *Nature* **483**, 311–314 (2012).

27. Park, J. A., Amri, C., Kwon, Y., Lee, J.-H. & Lee, T. Recent Advances in DNA Nanotechnology for Plasmonic Biosensor Construction. *Biosensors* **12**, 418 (2022).

28. Song, S., Jeon, M. J., Lee, J. U. & Sim, S. J. Recent advances in DNA-assembled plasmonic nanoarchitectures for biomedical applications. *TrAC Trends Anal. Chem.* **177**, 117784 (2024).

29. Duan, H., Wang, T., Su, Z., Pang, H. & Chen, C. Recent progress and challenges in plasmonic nanomaterials. *Nanotechnol. Rev.* **11**, 846–873 (2022).

30. Ngo, N. M., Tran, H.-V. & Lee, T. R. Plasmonic Nanostars: Systematic Review of their Synthesis and Applications. *ACS Appl. Nano Mater.* **5**, 14051–14091 (2022).

31. Wang, Y., Han, N., Li, X., Yu, S. & Xing, L. Artificial light-harvesting systems and their applications in photocatalysis and cell labeling. *ChemPhysMater* **1**, 281–293 (2022).

32. Klymchenko, A. S., Biswas, D. S. & Didier, P. Light-Harvesting Nanomaterials Based on Dyes for Energy Transfer and Amplified Biosensing. *Adv. Mater. Deerfield Beach Fla* e01237 (2025) doi:10.1002/adma.202501237.

33. Kundu, S. & Patra, A. Nanoscale Strategies for Light Harvesting. *Chem. Rev.* **117**, 712–757 (2017).

34. Li, C. *et al.* Scaffold-Free Efficient Light-Harvesting Nanoparticles Based on One-Pot Self-Assembly of Donor–Acceptor Aggregation-Induced Emission Luminogens. *ACS Appl. Nano Mater.* **7**, 24469–24476 (2024).

35. Jeon, H., Kim, Y. M., Han, S., Moon, H. C. & Lee, J. B. DNA Optoelectronics: Versatile Systems for On-Demand Functional Electrochemical Applications. *ACS Nano* **16**, 241–250 (2022).

36. Fathizadeh, S. & Nemati, F. DNA based nanoscale optoelectronic devices enabled by THz driven piezo vibrotronic effect. *Sci. Rep.* **15**, 29307 (2025).

37. Satyabola, D., Prasad, A., Yan, H. & Zhou, X. Bioinspired Photonic Systems Directed by Designer DNA Nanostructures. *ACS Appl. Opt. Mater.* **3**, 552–568 (2025).

38. Bush, J. *et al.* Synthesis of DNA Origami Scaffolds: Current and Emerging Strategies. *Molecules* **25**, 3386 (2020).

39. Shani, L. *et al.* DNA-assembled superconducting 3D nanoscale architectures. *Nat. Commun.* **11**, 5697 (2020).

40. Michelson, A. *et al.* Three-dimensional nanoscale metal, metal oxide, and semiconductor frameworks through DNA-programmable assembly and templating. *Sci. Adv.* https://doi.org/10.1126/sciadv.adl0604 (2024) doi:10.1126/sciadv.adl0604.

41. Gao, Y. *et al.* Reversible metamorphosis of hierarchical DNA–inorganic crystals. *Nat. Nanotechnol.* 1–9 (2025) doi:10.1038/s41565-025-02026-8.

42. Effects of chain flexibility on the properties of DNA hydrogels - Soft Matter (RSC Publishing). https://pubs.rsc.org/en/content/articlelanding/2016/sm/c6sm00283h.

43. Chen, T., Li, M. & Liu, J. π–π Stacking Interaction: A Nondestructive and Facile Means in Material Engineering for Bioapplications. *Cryst. Growth Des.* **18**, 2765–2783 (2018).

44. Thakuria, R., Nath, N. K. & Saha, B. K. The Nature and Applications of π–π Interactions: A Perspective. *Cryst. Growth Des.* **19**, 523–528 (2019).

45. González-Jiménez, M. *et al.* Observation of coherent delocalized phonon-like modes in DNA under physiological conditions. *Nat. Commun.* **7**, 11799 (2016).

46. Fathizadeh, S. Phonon-assisted nearly pure spin current in DNA molecular chains: a multifractal analysis. *Sci. Rep.* **13**, 21281 (2023).

47. Spin-phonon coupling in a double-stranded model of DNA - PubMed. https://pubmed.ncbi.nlm.nih.gov/37449581/.

48. Kurnia Suhendro, D., Yudiarsah, E. & Saleh, R. Effect of phonons and backbone disorder on electronic transport in DNA. *Phys. B Condens. Matter* **405**, 4806–4811 (2010).

49. Ojeda, J. H., Maiti, S. K., Laroze, D., Eramo, G. & Orellana, P. A. Effect of electron–phonon interaction on thermoelectric properties of a DNA molecule. *J. Chem. Phys.* **162**, 244115 (2025).

50. Starikov *, E. B. Electron–phonon coupling in DNA: a systematic study. *Philos. Mag.* **85**, 3435–3462 (2005).

51. Nesterova, I. V. & Nesterov, E. E. Rational Design of Highly Responsive pH Sensors Based on DNA i-Motif. *J. Am. Chem. Soc.* **136**, 8843–8846 (2014).

52. Nesterova, I. V., Elsiddieg, S. O. & Nesterov, E. E. Design and Evaluation of an i-Motif-Based Allosteric Control Mechanism in DNA-Hairpin Molecular Devices. *J. Phys. Chem. B* **117**, 10115–10121 (2013).

53. Chen, C. *et al.* Study of pH-Induced Folding and Unfolding Kinetics of the DNA i-Motif by Stopped-Flow Circular Dichroism. *Langmuir* **28**, 17743–17748 (2012).

54. Conrad, N., Kennedy, T., Fygenson, D. K. & Saleh, O. A. Increasing valence pushes DNA nanostar networks to the isostatic point. *Proc. Natl. Acad. Sci.* **116**, 7238–7243 (2019).

55. Ding, Y., Fleming, A. M., He, L. & Burrows, C. J. Unfolding Kinetics of the Human Telomere i-Motif Under a 10 pN Force Imposed by the α-Hemolysin Nanopore Identify Transient Folded-State Lifetimes at Physiological pH. *J. Am. Chem. Soc.* **137**, 9053–9060 (2015).

56. Baumgarten, K. & P. Tighe, B. Moduli and modes in the Mikado model. *Soft Matter* **17**, 10286–10293 (2021).

57. Chen, C. *et al.* Study of pH-Induced Folding and Unfolding Kinetics of the DNA i-Motif by Stopped-Flow Circular Dichroism. *Langmuir* **28**, 17743–17748 (2012).

58. ATTO 647N. *ATTO-TEC GmbH* https://www.atto-tec.com/ATTO-647N.html?language=en.

59. Grill, M. J., Kernes, J., Slepukhin, V. M., Wall, W. A. & Levine, A. J. Directed force propagation in semiflexible networks. *Soft Matter* **17**, 10223–10241 (2021).

60. Kumar, A., Quint, D. A. & Dasbiswas, K. Range and strength of mechanical interactions of force dipoles in elastic fiber networks. *Soft Matter* **19**, 5805–5823 (2023).

61. Lou, Y. Appetizer on soft matter physics concepts in mechanobiology. *Dev. Growth Differ.* **65**, 234–244 (2023).

62. van Doorn, J. M. *et al.* Propagation and attenuation of mechanical signals in ultrasoft 2D solids. *Sci. Adv.* **6**, eaba6601 (2020).

63. Force Propagation in Active Cytoskeletal Networks. https://arxiv.org/html/2401.04217v2.

64. Kubota, R. *et al.* Force generation by a propagating wave of supramolecular nanofibers. *Nat. Commun.* **11**, 3541 (2020).

65. Burlak, G. & Medina-Ángel, G. Dynamical Properties of Plasmon Polaritons in Nanorings Driven by Cassini-Ordered Emitters. *Nanomaterials* **15**, 576 (2025).

66. Guo, Y., Xu, Z., Curto, A. G., Zeng, Y.-J. & Van Thourhout, D. Plasmonic semiconductors: materials, tunability and applications. *Prog. Mater. Sci.* **138**, 101158 (2023).

67. Chung, T. *et al.* Nanoislands as plasmonic materials. *Nanoscale* **11**, 8651–8664 (2019).

68. Hossain, N. *et al.* Advances and significances of nanoparticles in semiconductor applications – A review. *Results Eng.* **19**, 101347 (2023).

69. Terahertz light confined to the nanoscale with hafnium dichalcogenides. *Nat. Mater.* **24**, 1688–1689 (2025).

70. Serra Gonzalez, M., Kavkani, P. H., Deshpande, R. A., Kadkhodazadeh, S. & Taboryski, R. A Correlative Study of Plasmonic Metasurfaces by Electron Energy-Loss Spectroscopy and Optical Spectroscopy: From Nanoscale Hotspots to Macroscale Optical Response. *Nano Lett.* **25**, 11979–11985 (2025).

Figures

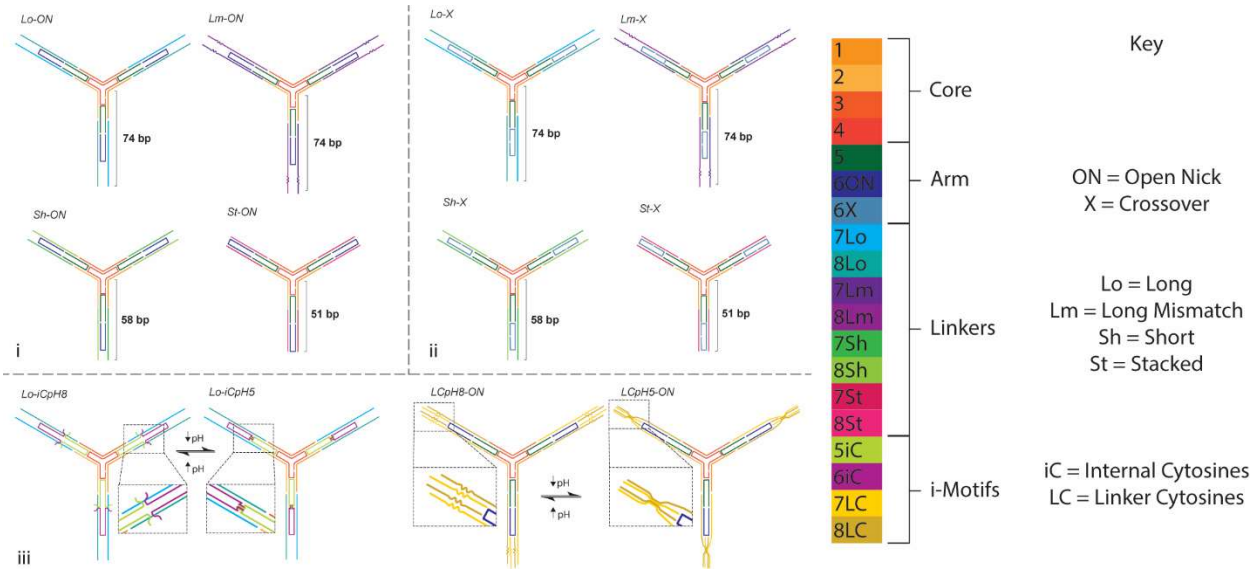

Figure 1

Depiction of the variable designs used in this study. The staple strands for all designs have 42 hybridizing bases while the 'Internal Cytosines' staple strands have additional cytosine bases spaced from the hybridizing region by a thymine base. The standard arm length used in 51 bp long which approximates to near 17 nanometers with up to an additional 7nm for the 21bp linkers (Lo and Lm) and slightly over 2nm for the 7bp linker (Sh) with 0 bp for the base-stacking 'linker'. This yields approximately 34-41nm between each vertex of two 'in-plane' crosslinked motifs. iii) pH- switchable analogues at high and low pH with insets which depict the i-motif formation. Shapes correlate to the 'innately' programmed analogues.

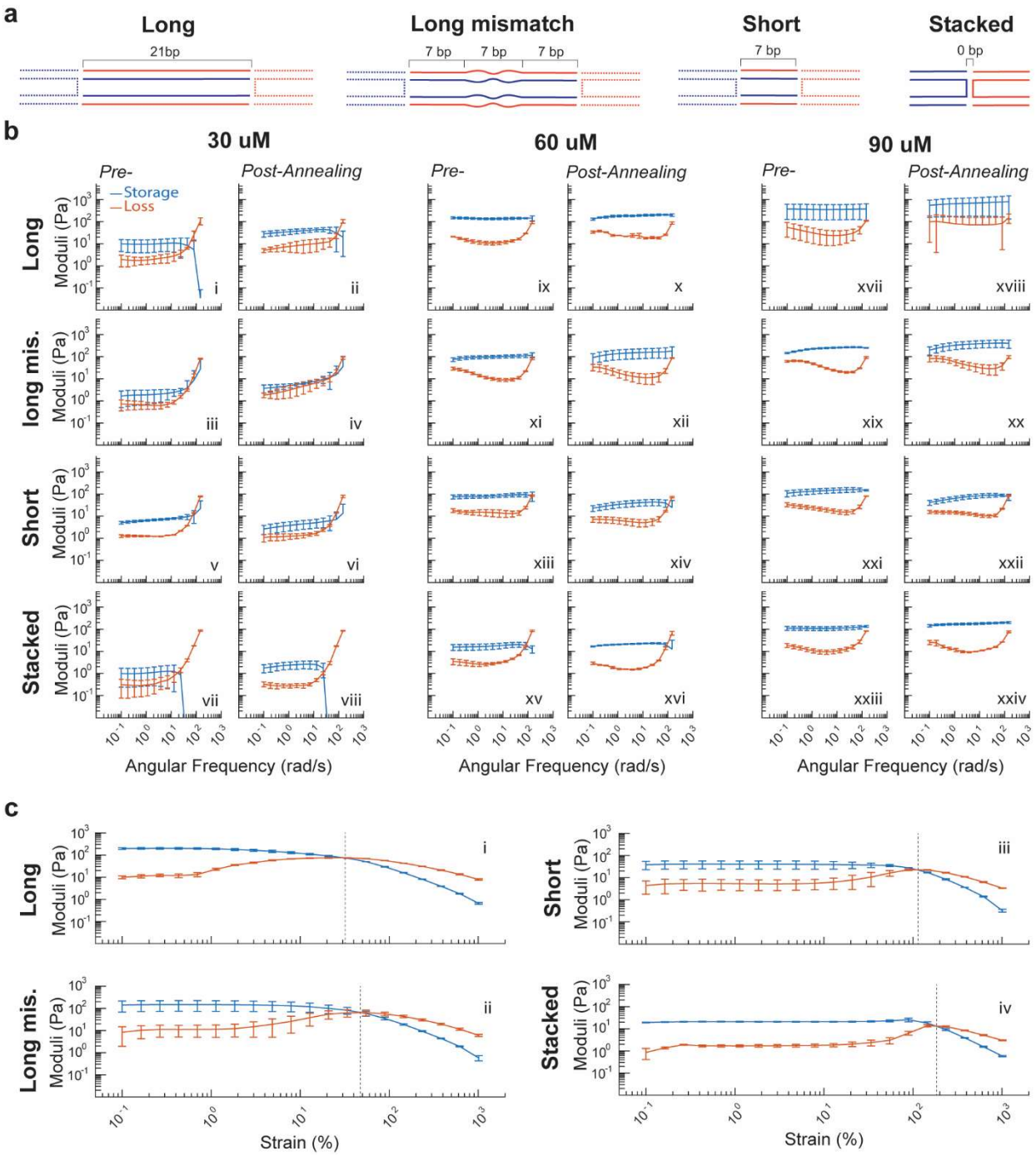

Figure 2

A) Frequency sweep rheological profiles for designs of the pliant arm and all 4 linkers at 3 concentrations of 30, 60, 90 uM. B) Strain sweep rheological profiles for design of the pliant arm and all 4 linkers at 60 uM.

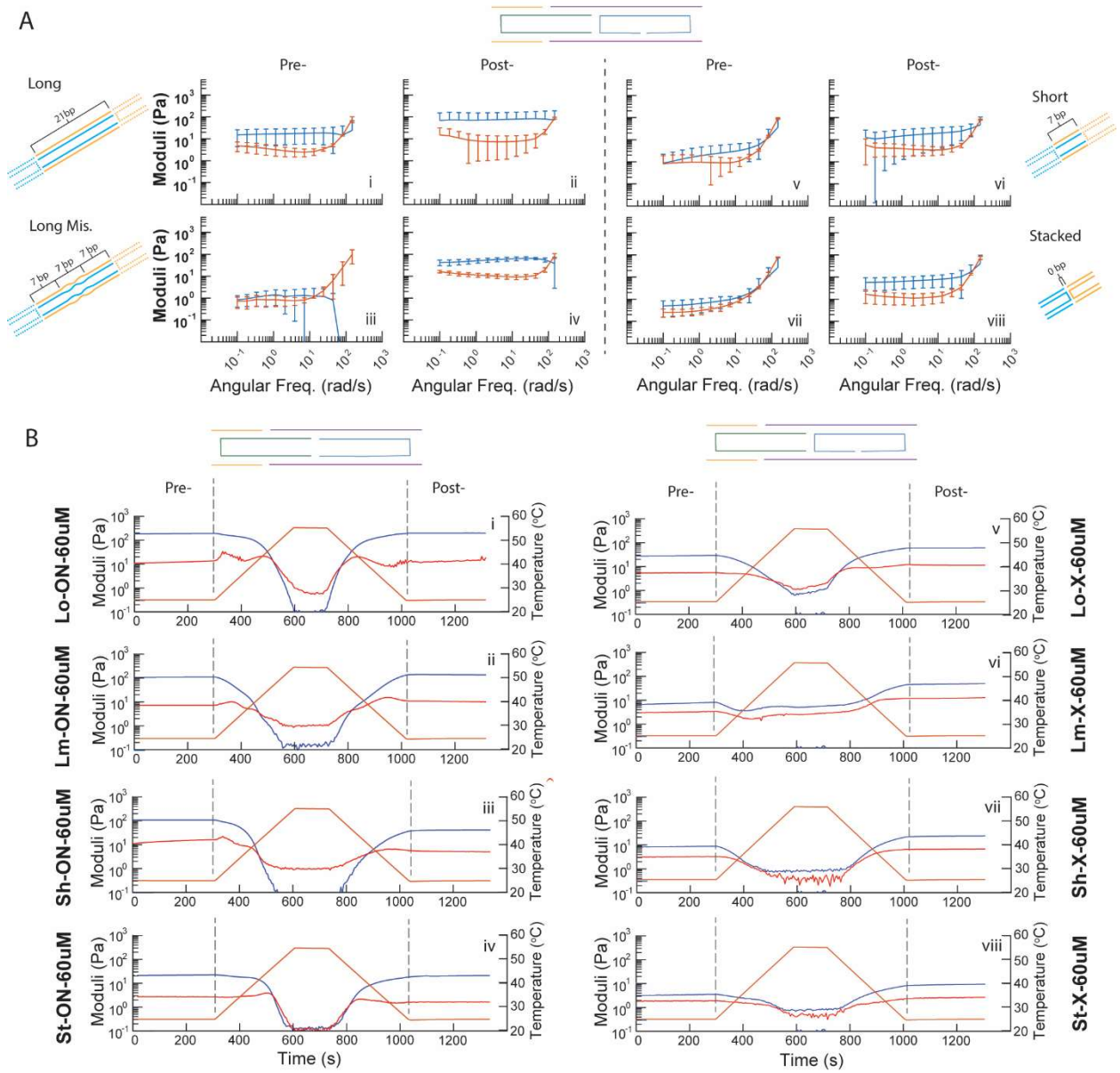

Figure 3

Frequency sweep and thermal rheological profiles for designs of the rigid arm with all 4 linkers at 60 uM. A) Pre- and Post- Heating/Cooling frequency sweep profiles (1% strain) designs with the closed nick 'rigid' arm (Lo-X, Lm-X, Sh-X, St-X) B) Heating/Cooling thermal profile of storage and loss modulus for open nick (ON - pliant) and closed nick, or crossover (X - rigid) arm.

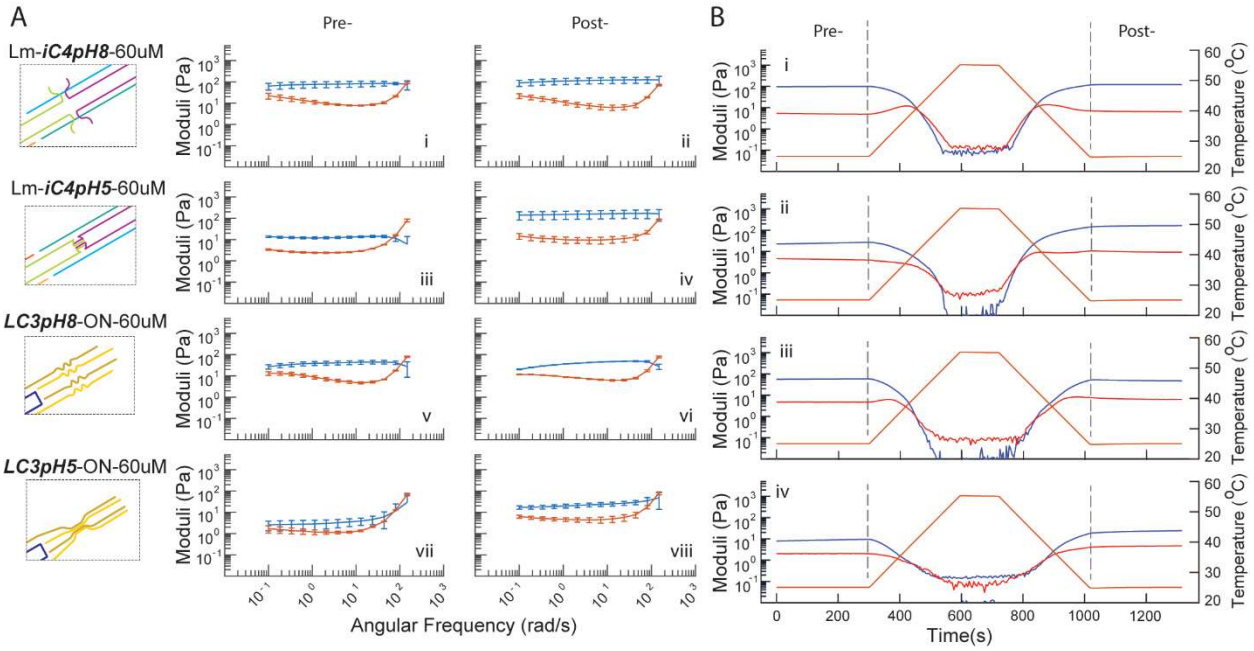

Figure 4

Frequency sweep and thermal profiles for designs including functional i-motifs inserted within the structure itself and within the linker itself, measured at both a pH of 5.0 and 8.0.

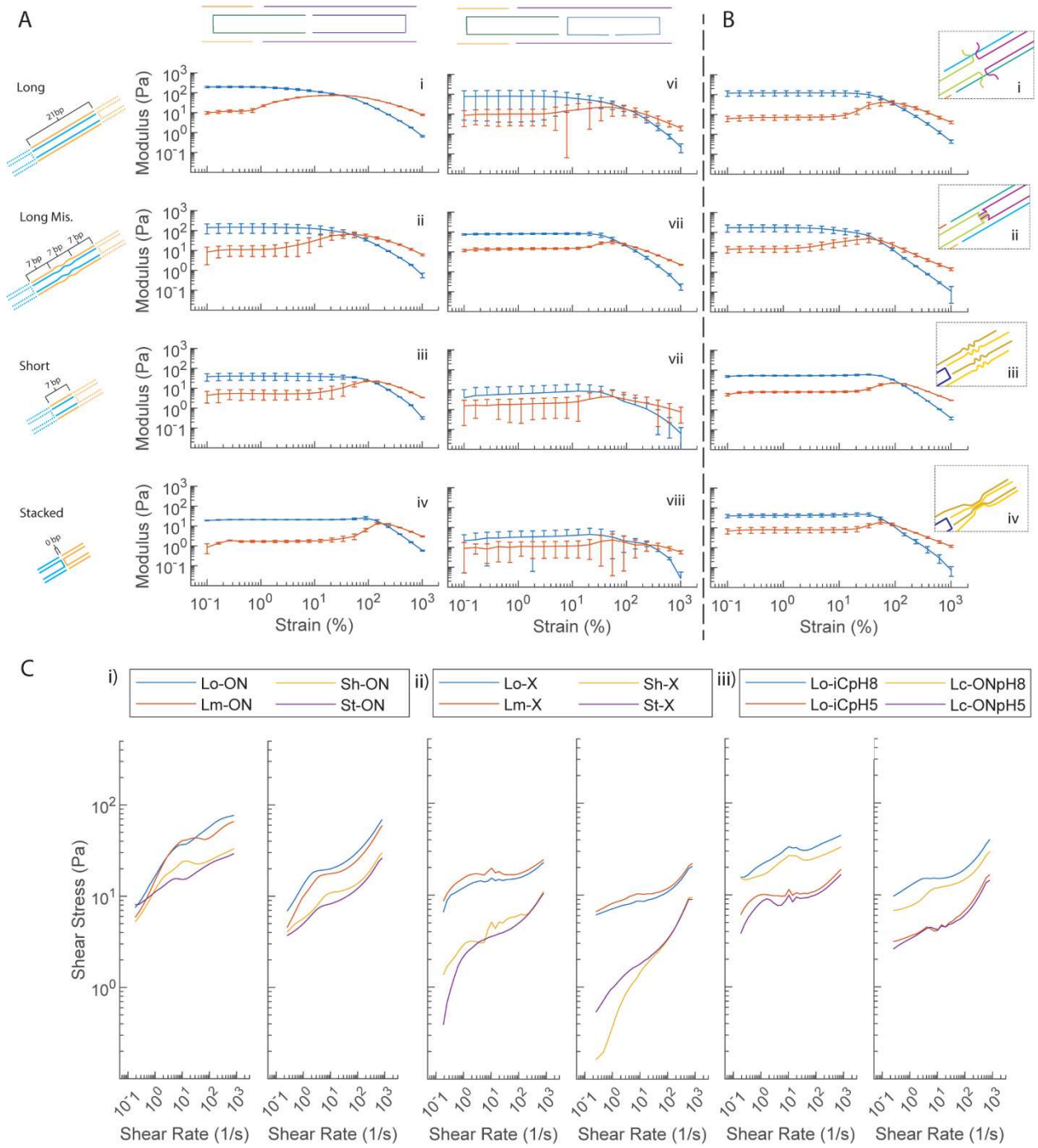

Figure 5

Strain sweep and shear rate rheological profiles for all designs at 60 uM. (Strain sweeps in the first column of panel A are identical data to that presented in Figure 2C reshown here for ease of comparison.)